WWR orig. June 12, 2009

Hysteresis and Interfacial Energies in Smooth-walled Microfluidic Channels

Yihong Liu[1], D. D. Nolte[1] and L. J. Pyrak-Nolte[1,2]

1. Dept. of Physics, Purdue University
2. Dept. of Earth and Atmospheric Sciences, Purdue University

Abstract:

Hysteresis in the capillary pressure – saturation relationship (P_c – S_w) for a porous medium has contributions from the complex geometry of the pore network as well as the physical chemistry of the grain surfaces. To isolate the role of wettability on hysteresis, we fabricated micro-fluidic cells that contain a single wedge-shaped channel that simulates a single pore throat. Using confocal microscopy of the three-dimensional interfaces under imbibition and drainage, we demonstrate an accurate balance between mechanical work and surface free energy that was evaluated using measured advancing and receding contact angles. The closed-loop mechanical work per surface water molecule is 95 kJ/mol, which is consistent with physisorption. Therefore, the hysteresis in the P_c – S_w relationship for a single pore throat is defined by advancing and receding contact angles that are controlled by dissipative surface adsorption chemistry.

1. Introduction

Hysteresis is a common property of the capillary pressure vs. saturation ($P_c - S_w$) behavior of porous media that prevents a unique description of the state of the porous system [*Bear*, 1972; *Dullien*, 1992; *Muccino, et al.*, 1998]. This ambiguity presents a challenge for upscaling theories of partial saturation that are applied to problems of sequestration, ground water remediation and hydrocarbon extraction [*Wu and Forsyth*, 2001; *Broje and Keller*, 2007; *Liu and Smirnov*, 2008; *Yoon, et al.*, 2008]. Several physical mechanisms contribute to $P_c - S_w$ hysteresis that raise questions of thermodynamic equilibrium, metastability and irreversibility. Hysteresis is influenced by the geometry of pores combined with the asymmetry of imbibition and drainage, and can be caused in random porous media by topological bifurcations as the mobile interface meets an obstruction and takes one path among a choice of paths. In addition, hysteresis is caused by changes in interfacial energies as the common point or line of two mobile phases sweeps across a solid interface.

Many experimental methods have been used to measure the IAV for natural and synthetic porous samples, such as nuclear magnetic resonance imaging (MRI) [*Packer, et al.*, 1998; *Zhang, et al.*, 2002], X-ray computed microtomography (CT) and synchrotron X-ray microtomography (SXM) [*Wildenschild, et al.*, 2002; *Culligan, et al.*, 2004; *Culligan, et al.*, 2006; *Costanza-Robinson, et al.*, 2008; *Porter, et al.*, 2010], and photoluminescent volumetric imaging (PVI) [*Montemagno and Gray*, 1995] as well as two-dimensional transparent micro-models that enable direct optical evaluation of the fluid distributions [*Cheng, et al.*, 2004; *Ovdat and Berkowitz*, 2006; *Chang, et al.*, 2009]. Two dimensional micro-models with random pore distributions were used to demonstrate

that the ambiguity of the hysteresis is lifted by the interfacial area per volume between the wetting and non-wetting phases (a_{wn}) [*Chen, et al.*, 2007; *Pyrak-Nolte, et al.*, 2008]. This previous work focused on thin 2D micro-models. The total area of the micro-porous patterns was 600 x 600 μm^2 and the sample thickness was approximately 1 or 2 μm. Interfacial length per area was investigated from optical images in the previous work [*Chen, et al.*, 2007; *Pyrak-Nolte, et al.*, 2008], but it was difficult to measure the contact angles and the full 3D interface between the fluids. In this paper, we provide a method to directly visualize the 3D interfaces and 3D fluid distributions using laser scanning confocal microscopy. This method has a resolution around or less than 1 μm, which makes it an excellent method to investigate micro-pore scale problems.

In complex porous structures, the capillary-dominated a_{wn} provides an additional variable for the description of the state of the system according to the thermodynamic theory developed by Hassanizadeh and Gray [*Hassanizadeh and Gray*, 1990; *Gray and Hassanizadeh*, 1991; *Hassanizadeh and Gray*, 1993]. Computational modeling and experimental validation consistent with the theory have been performed on various multiphase porous systems with complex geometries [*Cheng, et al.*, 2004; *Culligan, et al.*, 2004; *Chen, et al.*, 2007; *Joekar-Niasar, et al.*, 2008; *Niasar, et al.*, 2009; *Porter, et al.*, 2009]. Helland and Skjaeveland considered contact angle hysteresis to investigate the $P_c - S_w - a_{wn}$ relationship [Helland and Skjaeveland, 2007]. They found that contact angle hysteresis and fluid hinging resulted in a non-unique relationship among $P_c - S_w - a_{wn}$ for the complex geometry formed by a bundle of triangular tubes.

In this paper, we have fabricated a wedge channel to eliminate the geometrical contributions of the porous structures to the hysteresis and to simulate one throat in a

microporous medium. Capillary pressure – wetting phase saturation $P_c - S_w$ hysteresis was examined in the non-random micro-model consisting of smooth-walled channels. By employing confocal microscopy, the three-dimensional (3D) single interface in the wedge channel was imaged. The a_{wn} was measured and its dependence on the $P_c - S_w$ hysteresis was examined. From the 3D interface, transverse and axial contact angles were analyzed, and the relationship between the contact angle hysteresis and the $P_c - S_w$ hysteresis are discussed. The area under the $P_c - S_w$ scanning curves is related to the irreversible surface free energy change that occurs as the common line between the solid phase and the two mobile phases of liquid (water and air) moves along the interface.

2. Sample Fabrication and Data Acquisition

Micro-models were fabricated using a negative photoresist (SU-8) sandwiched between two cover glasses (18 x 18 mm^2). SU-8 is widely used in applications of micro-electro mechanical systems (MEMS), with high cross-linking performance, high-aspect-ratio and straight side-wall fabrication, and excellent chemical thermal resistance [*Shaw and Gelorme*, 1997; *Feng and Farris*, 2003; *Kawata and Hong-Bo*, 2003; *Teh, et al.*, 2005]. Two simple 'wedge-shaped' channels were fabricated by laser direct-writing two-photon polymerization (2PP) [*Liu, et al.*, 2010]. A 40 μm thick layer of SU-8 was spin-coated on a substrate and soft baked in an oven at 65°C and 95°C for 15 min and 30 min, respectively. A femtosecond laser with pulse energy of 1 nJ was employed to expose the microchannel, and an XYZ motion stage was programmed with an accuracy of 1 μm, which is consistent with the channel design. Smooth channel walls with high accuracy and low surface roughness were achieved through direct-writing 2PP that minimizes

contact angle variability caused by surface roughness. Following two-photon exposure, round inlet and outlet ports with diameters of 3 mm were exposed by a UV lamp with a power of 400 mW for 30 sec. After exposure, the sample was baked at 65°C and then 95°C for 10 min and 15 min, respectively, to cross-link the photoresist, and then gradually cooled to room temperature to avoid quenching residual stresses. The sample was developed in a commercial developer (Microchem) for 6 min, rinsed in isopropyl alcohol, and placed on a flat surface to dry. Two holes were drilled in the ports to introduce fluids, and the sample was sealed by a cover glass.

Top and bottom cover slips were coated with 5 μm thick SU-8 layers so that the micro channel was completely encased by the photoresist SU-8 to provide a homogeneous surface chemistry. The bottom layer was spin coated onto the cover glass, soft-baked in an oven, exposed by a UV lamp, and post-baked for cross-linking. After post-baking, the bottom layer of photoresist SU-8 had already polymerized and could not be exposed by the femtosecond laser. The 40 μm thick SU-8 layer was then spin-coated onto the bottom layer and the laser writing technique was used to fabricate the micro-channel. After developing the channel, a cover glass with the top layer was put on the channel to seal the micro-model. The sample was soft-baked on a hot plate at 65 ^{o}C and 95 ^{o}C for 1 min and 3 min, respectively. The entire micro-model was then exposed by a UV lamp for 10 sec and post-baked on a hot plate so that the top layer was also cross-linked. Therefore, the top and bottom layers were both polymerized, and all channel surfaces were made of polymerized SU-8. Two samples with the same geometric structures were fabricated according to the protocol above, and repeated drainage and imbibition scans were performed on both samples.

Data were acquired using a laser-scanning confocal microscope (Zeiss LSM 710), as shown in Figure Captions

Figure 1 that employed a pressure-controlled flow system. The micro-model was mounted on the sample holder. Two fluids, water (wetting phase), dyed with Alexa-fluor 488 with a concentration of 0.1 mg/ml, and air (non-wetting phase), were introduced into the micro-model through the holder from two reservoirs on either side of the wedge-shaped channel. We measured the surface tensions of de-ionized (DI) water with and without fluorescent dye using the du Noüy ring method at room temperature (23°C). The device was a Kruss Company tensiometer with an accuracy of ±0.1 mN/m Based on four measurements, the surface tension of the dyed water was on average only 0.25 mN/m (or 0.35%) less than that of DI water. This small difference may be caused by fluctuations in room temperature. The small difference in surface tension with and without dye establishes that the Alex-fluor has a negligible effect on the surface tension of the dyed water.

To control the water pressure, a syringe containing water with an end open to the atmosphere was mounted on a ring stand. The water pressure was determined by the height of the water level in the syringe, measured by a pressure transducer (Omega Engineering Inc. accuracy 0.01 psi / 69 Pa), and output to a display meter. To control the air pressure, a micrometer was used to adjust the air volume of an air-tight syringe. The air pressure was also monitored with a transducer and a display meter. Tygon Microbore tubing (Cole-Parmer) was used to connect the parts described above.

Confocal microscopy was used to acquire in-focus images from selective depths, to build an entire 3D interface from the acquired 2D images and to enable direct

measurement of the interfacial area. The data from a confocal stack can be used to view the data in several ways. Figure 2 shows examples of (2a) the fluorescent channel and orthogonal planes, (2b) a 3D interface reconstructed from one confocal stack, and (2c) an overlap image of the fluorescent and transparent channels. The optical section (full-width half-maximum of the point spread function in the z direction) is 1.4 μm, which is less than 1/25 of the depth of our microchannel. The transverse resolution is 1.19 μm/pixel.

Before the experiment, the wetting-phase reservoir of the flow system was flushed with the fluorescent water to eliminate air bubbles. Dyed water was introduced into the sample inlet through the channel contained in the sample holder. All experiments started with the wetting saturation equal to unity. As the pressure of the non-wetting phase (air) increased, the wetting phase was drained from the channel. During drainage, a stack of confocal images was scanned at 0.714 μm/step through the entire sample depth at each pressure, 0.01 ~ 0.04 psi/step (70 ~ 280 Pa/step). We waited at least 5 min after each pressure increment to establish mechanical equilibrium of the interface, and each confocal scan took about 1.5 min to complete at each pressure containing 85 frames. The same procedure was repeated for all imbibition and drainage scans.

3. Results

Volume saturations of the wetting phase and interfacial area per volume (a_{wn}) between the wetting and non-wetting phases were quantified using image analysis and are shown in Figure 3. The fluorescent pixels in the micro-channel in the confocal images are the wetting phase. To calculate the wetting phase volume, the fluorescent pixels are summed over all images acquired for a single stack (i.e., at a single pressure). The

channel volume is equal to the wetting phase volume when the channel is fully saturated with fluorescent water. From the saturated data, we reconstructed the 3D structure of the wedge-shaped channel using the interface between the fluorescent and dark pixels that corresponds to the interface between the wetting phase (water) and the solid phase (the SU-8 channel). After acquiring the channel structure, the wetting (water) / non-wetting phase (air) interface was determined from the fluorescent / dark pixels in the micro-channel, respectively. From the fluorescent channel images, no fluid was observed in the corner of the channel nor were any water films observed. Thus, a_{wn} represents the interfacial area between bulk wetting and non-wetting fluids. The 3D wetting– non-wetting interface was assembled from the 2D interfaces analyzed from confocal images at successive channel depths. The interfacial area A_{wn} is the integral of the 3D wetting–non-wetting interface. The interfacial area per volume, a_{wn} in Figure 4 is defined as the interfacial area A_{wn} divided by the channel volume V_{ch}. The capillary pressure in Figures 3 and 4 is the difference between the air and water pressures measured by the two pressure transducers. The non-monotonic behavior of $a_{wn} - S_w$ at high saturation (Figure 4b) results from the difference in advancing and receding contact angles for imbibition and drainage. Because the sample contains only one pore throat, the number of pixels that define the interface at very low saturations is not sufficient to resolve the hysteresis at low saturation.

In Figure 4a, the capillary pressure as a function of wetting-phase saturation follows two different main curves during imbibition and drainage. The hysteretic dependence of capillary pressure on saturation that is commonly observed in porous media with complex geometry is observed here for the simple wedge-shaped channel in

our experiments. In the P_c - S_w - a_{wn} space, data points of drainage and imbibition scans form a 3D surface as shown in Figure 3. We determined that the drainage and imbibition surfaces are identical to within ±13% using the method reported by Chen et al. [*Chen, et al.*, 2007]. In this approach, a surface was fitted to the drainage data points in the P_c - S_w - a_{wn} space. The a_{wn} between the wetting and non-wetting phases of the imbibition data points were calculated as a function of P_c and S_w by interpolating the fitted drainage surface. Similarly, the a_{wn} of the drainage data points were calculated by interpolation of a fitted imbibition surface. The uniqueness of the imbibition and drainage surfaces was determined from the ratio, R, of the measured a_{wn}^{data} to the calculated a_{wn}^{cal}, given by

$$R = \frac{a_{wn}^{data}(P_c, S_w)}{a_{wn}^{cal}(P_c, S_w)} \tag{1}$$

The mean value of R is 0.9981 and the standard deviation is approximately 0.13. Therefore the drainage and imbibition surfaces are identical to within ±13%. R as a function of a_{wn}^{data} is shown in Figure 5a. The unique surface fitted to imbibition and drainage data is shown in Figure 5b. This unique surface makes the hysteretic relationships among P_c, S_w and a_{wn} invertible. Helland & Skjaeveland, (2007) found from simulations that contact angle hysteresis affects the uniqueness of the $P_c - S_w - a_{wn}$. However, our measurements were made only on a single pore throat while their study involved the complex geometry of a bundle of triangular tubes.

Figure 6b shows a comparison of the measured and the calculated capillary pressures. The calculated capillary pressure is given by

$$P_c = \gamma (k_1 + k_2) \tag{2}$$

where γ = 0.073 N/ m is the surface tension of water on SU-8 in air [*Tanaka, et al.*, 1993; *del Campo and Greiner*, 2007]; k_1 and k_2 are the curvatures of the interface on the x – y and z – y planes, respectively (Figure 6a). Interfaces in a plane are fit to the arc of a circle, and the radius is acquired by averaging the distances from the center to the points on the interface. 3D interfaces are extracted from the stacks of confocal images allowing the curvatures in the z – y plane to be analyzed and included in the total capillary pressure. The calculated capillary pressure has a similar range as the measured pressure, but deviations are caused by the confocal resolution and the finite number of interface pixels.

The error bars in Figure 6b combine the errors from confocal acquisition and the data analysis algorithm. To simulate confocal acquisition error, point spread functions on the x-y and z-y planes were used to calculate the convolutions of a given interface with a known geometry. The convolved images were then used to calculate parameters such as curvature and contact angle through the data analysis algorithm. Finally the error was determined by comparing the calculated value to the known geometry. The errors in x-y plane are larger at low water saturation than for high water saturation because the channel narrows resulting in fewer pixels along the interface.

Figure 7 shows the hysteresis of the contact angle as a function of wetting-phase saturation during imbibition and drainage scans. The contact angle analysis is based on the images on the middle x – y plane and the middle z – y plane (Figure 6a) using the same algorithm to calculate curvatures. The center of the circle fit to the interface is used to calculate the contact angle shown in Figure 7c. The error bars in Figures 7a & 7b are calculated from the error analysis algorithm described in the last paragraph. The x-y

plane contact angle hysteresis $\Delta\theta = \theta_a - \theta_r$ is approximately 30°, where the advancing contact angle θ_a is approximately 70° and the receding angle θ_r is approximately 40°. The z-y plane contact angle hysteresis $\Delta\theta = \theta_a - \theta_r$ is also approximately 30°, but the advancing contact angle θ_a is approximately 87° and the receding angle θ_r is approximately 60°. The advancing and receding contact angles measured in the two orthogonal planes differ by roughly 17^o-20^o. This difference is attributed the reduced resolution in the z-y plane. While we accounted for the point spread function of the laser, some systematic errors may remain. For instance, the signal to noise ratio of the confocal scan increases as the imaging plane goes deeper in a sample. This causes larger error in the z direction than in the x and y directions for the 3D interface reconstruction.

To verify mechanical equilibrium in the measurements, a relaxation experiment was performed with the same flow setup under an optical microscope. One optical image was taken every 4 min while the water and air pressure were maintained at 380 Pa and 3250 Pa, respectively. Area saturations and radii of the 2D interfaces were analyzed using the same algorithm and the results are shown in Figure 8. The relaxation time factors τ_s = 168 min and τ_r = 165 min were acquired by fitting an exponentially decaying function to the radius and saturation versus time data. Over 5 hours, the saturation decreased by only 0.01. The results indicate an extremely long-term and small-amplitude relaxation. For instance, the saturation difference between imbibition and drainage in the 1st experimental loop is $\Delta S_w = S_w^{dr} - S_w^{im} \sim 0.9 - 0.3 = 0.6$, which is 60 times larger than the change in saturation 0.01 from relaxation over the 5-hour period. Therefore, measurements of hysteresis from imbibition and drainage scans are in quasi-static mechanical equilibrium. While we cannot establish whether the system is in

thermodynamic equilibrium, we make a working definition that our experiments are performed in effective equilibrium (i.e., in a metastable equilibrium), meaning that large transients decay rapidly relative to the time between pressure steps, and long-term relaxation is not significant.

4. Discussion

The capillary pressure – saturation hysteresis, widely known in multiphase occupancy of porous media, has not been previously measured in 3D in a simple wedge-shaped channel that isolates the behavior of a single throat. Although complex geometry and bifurcations are important contributors to the hysteresis in the $P_c - S_w$ relationship for multiphase flow in porous media [*Gray*, 1999; *Niasar, et al.*, 2009], in our study, the geometrical contribution has been eliminated. Therefore, the phase occupancy is dominated only by the surface tension, and thus the hysteresis must be entirely determined by the surface chemistry.

In Figures 7a and 7b, contact angles on the x-y and z-y plane show hysteretic dependence on wetting phase saturation. Advancing and receding contact angles reflect the balance of the surface tensions of the wetting, non-wetting, and solid phases during liquid imbibition and drainage, respectively. Capillary pressure – saturation ($P_c - S_w$) hysteresis was simulated assuming that the hysteresis is controlled entirely by contact angle hysteresis (shown in Figure 4a as the blue curves with error bars). The x-y and z-y curvatures during imbibition and drainage were calculated at a given saturation from the mean values of the advancing and receding contact angles, respectively, and the capillary pressure P_c was calculated from the curvatures using Eq. (2). The error bars of the

simulated capillary pressure are based on errors associated with the confocal point-spread functions and the data analysis algorithm as described earlier. This error analysis also quantified the error associated with determining the contact angle and the x-y and z-y middle plane curvatures. Errors in the measurements of the interfacial curvature result in an error in the calculated pressure.

In Figure 4a, the simulation compares favorably with the experimental $P_c - S_w$ imbibition and drainage, except for saturations less than 0.1 when the interface approaches the small outlet of the wedge-shaped channel where the aspect ratio of the channel (width to height ratio) approaches unity and the uncertainty in the measurement is largest. *Therefore, in this simple channel geometry that simulates a single pore throat, the hysteresis in the advancing and receding contact angle uniquely determines the hysteresis in* $P_c - S_w$*.*

In complex two-phase porous systems, the interfacial area a_{wn} between the wetting and non-wetting phases is an important variable that is capable of resolving the capillary pressure – saturation ($P_c - S_w$) hysteresis [*Chen, et al.*, 2007]. In our wedge shaped channel a_{wn} again functions as a third variable that forms a unique surface with P_c and S_w. However, in this simple throat geometry, the hysteresis in a_{wn} is determined uniquely by the contact angles. *Therefore, while* a_{wn} *does perform the same function of lifting the* $P_c - S_w$ *hysteresis as in a complex geometry, it uniquely depends on the hysteretic contact angles, and hence is not an independent variable.*

To investigate interfacial energy in the smooth-walled channel, we compare the surface free energy F with external work W by analyzing the experimental data of the two samples. The capillary pressure – saturation $P_c - S_w$ graph was converted to a $P - V$

diagram by setting $V_w = V_{ch} S_w$, where V_{ch} is the channel volume. Increments in the work done during imbibition and drainage cycles were calculated from

$$\Delta W = (P_w - P_n)\,\Delta V_w = -P_c\,\Delta V_w = -P_c\,V_{ch}\,\Delta S_w \tag{3}$$

with accuracy of order $O(\Delta V/V) \sim 10^{-7}$. In our isothermal system, the surface free energy is given by

$$F = \Sigma \sigma_i A_i \tag{4}$$

where A_i are the interfacial areas and σ_i are the surface tensions. Thus

$$\Delta F = \sigma_{wn}\Delta A_{wn} + \sigma_{sw}\Delta A_{sw} + \sigma_{sn}\Delta A_{sn} \tag{5}$$

where w, n, and s represent the wetting phase (water), non-wetting phase (air), and solid phase (SU-8) [*Morrow*, 1970]. Because the sum of the solid – wetting interfacial area A_{sw} and the solid – non-wetting interfacial area A_{sn} is equal to the surface area of solid phase A_s (a constant) then

$$\Delta A_{sw} = -\Delta A_{sn} \tag{6}$$

The force balance at a common line is given by

$$\sigma_{wn} \cos\,\theta_{a,r} = \sigma_{sn} - \sigma_{sw} \tag{7}$$

where w, n, and s represent the wetting, non-wetting phase, and solid phases, σ is the surface tension between phases, and $\theta_{a,r}$ is the advancing or receding contact angles. Substituting Eq. (6) and (7) into Eq. (5), yields

$$\Delta F = \sigma_{wn}\Delta A_{wn} + \sigma_{wn} \cos\,\theta_{a,r}\,\Delta A_{sn}, \tag{8}$$

The interfacial areas A_{wn} and A_{sn} are calculated from the wetting phase saturation S_w acquired from the experiments. The surface free energy calculation included the contact angle hysteresis by substituting θ with the advancing contact angle (70°) during imbibition and receding contact angle (40°) during drainage. The relationship of the

external work and surface free energy is shown in Figure 9. The data fit a straight line $\Delta W = \Delta F$ with R = 0.995. *This demonstrates that the mechanical work accurately balances the change in surface free energy when the surface free energy is evaluated using the advancing and receding contact angles.*

Hysteresis indicates irreversible energy dissipation occurring as the common line sweeps across the solid interface during the scanning loops. The total energy cost E_{cost} of a closed scanning loop was calculated from the area of the $P_c - S_w$ graph enclosed by the loop. The solid surface area involved in the loops was calculated by measuring the absolute value of ΔA_{sw} for the loop. By fitting a linear relationship between E_{cost} and ΔA_{sw} for 6 scanning loops, the surface energy was calculated to be 164 mJ/m^2. This value can be compared with values for physical adsorption. The SU-8 used in our experiments is dissolved in γ-butyrolactone (GBL), and the disperse part of the surface energy, determined by the van der Waals force, is 39 mN/m [*Walther, et al.*, 2007]. The work required per unit area to overcome the van der Waals attraction is 78 mJ/m^2 [*Butt and Kappl*, 2010], which is approximately half of the measured work. In addition to the van der Waals energy, chemical bonding also contributes to adhesion. To make this comparison, the mechanical work is converted to energy per mole of surface water molecules for the scanning loops. The number of water molecules per area is

$$\left(\frac{1000 g / m^3}{18 g / mol} \; 6.67 x 10^{23} \right)^{2/3} \approx 10^{17} \, molecules / m^2 \qquad (9)$$

and the conversion of the mechanical work to energy per mole of surface water molecules for the scanning loops is

$$\frac{164x10^{-3}\,J/m^2}{10^{17}\,molecules/m^2}\;6.67x10^{23} = 95\,kJ/mol \tag{10}$$

Hydrogen bonding between water and the SU-8 surface has contributions from O—H···:O (30 kJ/mol) and HO—H···:OH^{+3} (18.4 kJ/mol) [*Speakman*, 1975; *Markovitch and Agmon*, 2007]. The combination of these energies is approximately half of the surface energy calculated by the mechanical work in the hysteresis loop. *Therefore, the irreversible mechanical work around the hysteresis loop, which is balanced by the surface free energy evaluated with the hysteretic advancing and receding contact angles, is consistent with physical adsorption and hydrogen bond energies of water on the SU8 surface.*

5. Conclusions

In conclusion, we have fabricated smooth-walled wedge microchannels using two-photon laser machining of the polymer SU-8 to test the origins of hysteresis in a single pore throat. The interfaces were measured in three dimensions using confocal microscopy during imbibition and drainage scans for a two-phase flow system (water and air). Hysteresis was observed on all projection planes of the P_c, S_w and a_{wn} space, with a unique and invertible surface. However, all projected hysteresis curves were completely characterized by the geometry of the interfaces when considering the difference between the advancing and receding contact angles, which are approximately 70^o and 30^o, respectively. In addition to these geometric analyses, we established that there is an accurate energy balance between the mechanical work performed on the system and the change in the surface free energy that was evaluated using the different advancing and receding contact angles. Therefore, we have demonstrated conclusively that the origin of hysteresis in this single channel rests on the difference between the advancing and

receding contact angles. To uncover the origins of *this* difference, we compared the energy dissipation in the scanning loops with chemical energies for water adsorption on SU8 through van der Waals attraction and hydrogen bonding. The dissipated energy and chemical energies agree within the accuracy of our estimates. The results of this paper are valid within the condition of mechanical equilibrium that was established by testing the long-term stability of the interfaces over many hours. While the interfaces may not be in ideal thermodynamic equilibrium, they are certainly in a metastable equilibrium, which is the relevant condition for most laboratory experiments and for practical applications in the field.

6. Acknowledgment

This research is supported by the National Science Foundation (0911284-EAR). The authors also wish to acknowledge support from the Lab Directed Research and Development (LDRD) program at Sandia National Laboratories. Sandia is a multiprogram laboratory operated by Sandia Corporation, a Lockheed Martin Company, for the United States Department of Energy's National Nuclear Security Administration under Contract DE-AC04-94AL85000.

7. References

Bear, J. (1972), *Dynamics of Fluids in Porous Media*, Dover, Mineola, New York.

Broje, V., and A. A. Keller (2007), Interfacial interactions between hydrocarbon liquids and solid surfaces used in mechanical oil spill recovery, *Journal of Colloid and Interface Science*, *305*, 286-292, DOI: 10.1016/j.jcis.2006.09.078.

Butt, H.-J., and M. Kappl (2010), Surface and Interfacial Forces, *Wiley-VCH Verlag GmbH & Co. KGaA*, *ISBN: 978-3-527-40849-8*, P5-54.

Chang, L. C., J. P. Tsai, H. Y. Shan, and H. H. Chen (2009), Experimental study on imbibition displacement mechanisms of two-phase fluid using micro model, *Environmental Earth Sciences*, *59*, 901-911, DOI: 10.1007/s12665-009-0085-6.

Chen, D. Q., L. J. Pyrak-Nolte, J. Griffin, and N. J. Giordano (2007), Measurement of interfacial area per volume for drainage and imbibition, *Water Resources Research*, *43*, DOI: 10.1029/2007wr006021.

Cheng, J. T., L. J. Pyrak-Nolte, D. D. Nolte, and N. J. Giordano (2004), Linking pressure and saturation through interfacial areas in porous media, *Geophys. Res. Lett.*, *31*, DOI: 10.1029/2003gl019282.

Costanza-Robinson, M. S., K. H. Harrold, and R. M. Lieb-Lappen (2008), X-ray microtomography determination of air-water interfacial area-water saturation relationships in sandy porous media, *Environmental Science & Technology*, *42*, 2949-2956, DOI: 10.1021/es072080d.

Culligan, K. A., D. Wildenschild, B. S. B. Christensen, W. G. Gray, and M. L. Rivers (2006), Pore-scale characteristics of multiphase flow in porous media: A comparison of air-water and oil-water experiments, *Advances in Water Resources*, *29*, 227-238, DOI: 10.1016/j.advwatres.2005.03.021.

Culligan, K. A., D. Wildenschild, B. S. B. Christensen, W. G. Gray, M. L. Rivers, and A. F. B. Tompson (2004), Interfacial area measurements for unsaturated flow through a porous medium, *Water Resources Research*, *40*, W12413-12411 to W12413-12412.

del Campo, A., and C. Greiner (2007), SU-8: a photoresist for high-aspect-ratio and 3D submicron lithography, *Journal of Micromechanics and Microengineering*, *17*, R81-R95, DOI: 10.1088/0960-1317/17/6/r01.

Dullien, F. A. L. (1992), *Porous Media: Fluid Transport and Pore Structure*, Academic, San Diego, CA.

Feng, R., and R. J. Farris (2003), Influence of processing conditions on the thermal and mechanical properties of SU8 negative photoresist coatings, *Journal of Micromechanics and Microengineering*, *13*, 80-88.

Gray, W. G. (1999), Thermodynamics and constitutive theory for multiphase porous-media flow considering internal geometric constraints, *Advances in Water Resources*, *22*, 521-547.

Gray, W. G., and S. M. Hassanizadeh (1991), Unsaturated Flow Theory Including Interfacial Phenomena, *Water Resources Research*, *27*, 1855-1863.

Hassanizadeh, S. M., and W. G. Gray (1990), Mechanics and Thermodynamics of Multiphase Flow in Porous-Media Including Interphase Boundaries, *Advances in Water Resources*, *13*, 169-186.

Hassanizadeh, S. M., and W. G. Gray (1993), Thermodynamic Basis of Capillary-Pressure in Porous-Media, *Water Resources Research*, *29*, 3389-3405.

Helland, J. O., and S. M. Skjaeveland (2007), Relationship between capillary pressure, saturation, and interfacial area from a model of mixed-wet triangular tubes, *Water Resources Research*, *43*, DOI: 10.1029/2006wr005698, (W12s10)

Joekar-Niasar, V., S. M. Hassanizadeh, and A. Leijnse (2008), Insights into the relationships among capillary pressure, saturation, interfacial area and relative permeability using pore-network modeling, *Transport in Porous Media*, *74*, 201-219, DOI: 10.1007/s11242-007-9191-7.

Kawata, S., and S. Hong-Bo (2003), Two-photon photopolymerization as a tool for making micro-devices, *Applied Surface Science*, *208-209*, 153-158.
Liu, G. X., and A. V. Smirnov (2008), Modeling of carbon sequestration in coal-beds: A variable saturated simulation, *Energy Conversion and Management*, *49*, 2849-2858, DOI: 10.1016/j.enconman.2008.03.007.
Liu, Y., L. J. Pyrak-Nolte, and D. D. Nolte (2010), Large-format Fabrication by Two-Photon Polymerization in SU-8, *Applied Physics A*, DOI: 10.1007/s00339-010-5735-8.
Markovitch, O., and N. Agmon (2007), Structure and energetics of the hydronium hydration shells, *Journal of Physical Chemistry A*, *111*, 2253-2256.
Montemagno, C. D., and W. G. Gray (1995), Photoluminescent Volumetric Imaging - a Technique for the Exploration of Multiphase Flow and Transport in Porous-Media, *Geophysical Research Letters*, *22*, 425-428.
Morrow, N. R. (1970), Physics and Thermodynamics of Capillary Action in Porous Media, *Industrial and Engineering Chemistry*, *62*, 32-&.
Muccino, J. C., W. G. Gray, and L. A. Ferrand (1998), Toward an improved understanding of multiphase flow in porous media, *Reviews of Geophysics*, *36*, 401-422.
Niasar, V. J., S. M. Hassanizadeh, L. J. Pyrak-Nolte, and C. Berentsen (2009), Simulating drainage and imbibition experiments in a high-porosity micromodel using an unstructured pore network model, *Water Resources Research*, *45*, DOI: 10.1029/2007wr006641.
Ovdat, H., and B. Berkowitz (2006), Pore-scale study of drainage displacement under combined capillary and gravity effects in index-matched porous media, *Water Resources Research*, *42*, DOI: 10.1029/2005wr004553.
Packer, K. J., S. Stapf, J. J. Tessier, and R. A. Damion (1998), The characterisation of fluid transport in porous solids by means of pulsed magnetic field gradient NMR, *Magn. Reson. Imaging*, *16*, 463-469.
Porter, M. L., M. G. Schaap, and D. Wildenschild (2009), Lattice-Boltzmann simulations of the capillary pressure-saturation-interfacial area relationship for porous media, *Advances in Water Resources*, *32*, 1632-1640, DOI: 10.1016/j.advwatres.2009.08.009.
Porter, M. L., D. Wildenschild, G. Grant, and J. I. Gerhard (2010), Measurement and prediction of the relationship between capillary pressure, saturation, and interfacial area in a NAPL-water-glass bead system, *Water Resources Research*, *46*, DOI: 10.1029/2009wr007786.
Pyrak-Nolte, L. J., D. D. Nolte, D. Q. Chen, and N. J. Giordano (2008), Relating capillary pressure to interfacial areas, *Water Resources Research*, *44*, DOI: 10.1029/2007wr006434.
Shaw, J. M., and J. D. Gelorme (1997), Negative photoresists for optical lithography, *IBM Journal of Research & Development*, *41*, 81.
Speakman, J. C. (1975), The hydrogen bond and other intermolecular forces, *The Chemical Society (London) ISBN-13: 978-0851869193*.
Tanaka, T., M. Morigami, and N. Atoda (1993), Mechanism of Resist Pattern Collapse During Development Process, *Japanese Journal of Applied Physics Part 1-Regular Papers Short Notes & Review Papers*, *32*, 6059-6064.

Teh, W. H., U. Durig, U. Drechsler, C. G. Smith, and H. J. Guntherodt (2005), Effect of low numerical-aperture femtosecond two-photon absorption on (SU-8) resist for ultrahigh-aspect-ratio microstereolithography, *Journal of Applied Physics*, *97*, 54907-54901.

Walther, F., P. Davydovskaya, S. Zurcher, M. Kaiser, H. Herberg, A. M. Gigler, and R. W. Stark (2007), Stability of the hydrophilic behavior of oxygen plasma activated SU-8, *Journal of Micromechanics and Microengineering*, *17*, 524-531.

Wildenschild, D., J. W. Hopmans, C. M. P. Vaz, M. L. Rivers, D. Rikard, and B. S. B. Christensen (2002), Using X-ray computed tomography in hydrology: systems, resolutions, and limitations, *J. Hydrol.*, *267*, 285-297.

Wu, Y. S., and P. A. Forsyth (2001), On the selection of primary variables in numerical formulation for modeling multiphase flow in porous media, *Journal of Contaminant Hydrology*, *48*, 277-304.

Yoon, H., C. J. Werth, A. J. Valocchi, and M. Oostrom (2008), Impact of nonaqueous phase liquid (NAPL) source zone architecture on mass removal mechanisms in strongly layered heterogeneous porous media during soil vapor extraction, *Journal of Contaminant Hydrology*, *100*, 58-71, DOI: 10.1016/j.jconhyd.2008.05.006.

Zhang, C. Y., C. J. Werth, and A. G. Webb (2002), A magnetic resonance imaging study of dense nonaqueous phase liquid dissolution from angular porous media, *Environ. Sci. Technol.*, *36*, 3310-3317, DOI: 10.1021/es011497v.

Figure Captions

Figure 1. Sketch of the experimental set-up for the pressure controlled two-phase flow system with data acquisition by confocal microscope.

Figure 2. (a) An example of a confocal image and orthogonal planes. The wetting phase (water) was labeled with a fluorescent dye Alexa-fluor 488 (Invitrogen), concentration 0.1 mg/ml, excited by a laser at a wavelength of 488 nm, and detected by a photomultiplier tube with a band pass filter between 495 ~ 562 nm. (b) The 3D reconstruction from one stack of confocal images. (c) An overlap image with transparent and fluorescent channel of the micro channel. Channel dimensions are on the figure.

Figure 3. The relationship between wetting phase saturation, measured capillary pressure, and interfacial area per volume (a_{wn}) for several imbibition and drainage scans.

Solid lines and circles represent sample 1 (S1). Dashed lines and hollow circles represent sample 2 (S2). Different colors show different scan loops.

Figure 4. 2D Projections from Figure 3. The markers and colors are the same as those in Figure 3. The blue curves with error bars in (a) indicate the simulation of pressure – saturation hysteresis calculated using advancing and receding contact angles during imbibition and drainage scans.

Figure 5. (a) The ratio of measured a_{wn} to calculated a_{wn} from the interpolated surfaces as a function of measured a_{wn}. (b) The 3D fitted surface in P_c - S_w - a_{wn} space. The blue circles represent experimental data points.

Figure 6. (a) 3D interfaces and channel structures extracted from confocal images. The resolution is 1.19 μm/pixel on the x–y plane and 0.714 μm/step in the z direction. (b) Capillary pressures measured from transducers compared with pressures calculated from curvatures on x-y and z-y planes using Eq. (2). The line has a slope of unity.

Figure 7. The hysteretic dependence of (a) x – y middle plane contact angle and (b) z – y middle plane contact angle on wetting phase saturation. Different error bars for the x-y and z-y contact angles are due to different point spread functions for the x, y and z axes. (c) A sketch of the method used to determine contact angle (θ) superimposed on an image of the partially water-saturated wedge-shaped channel.

Figure 8. The relaxation of radius (red solid circle) and wetting phase saturation (blue empty square) as a function of time. The curve was fit to an exponentially decaying function.

Figure 9. The external work ΔW calculated from the area under the $P_c - S_w$ curve (Figure 4a) as a function of the surface free energy ΔF calculated from variation of surface ΔA_{ws} and ΔA_{wn}.

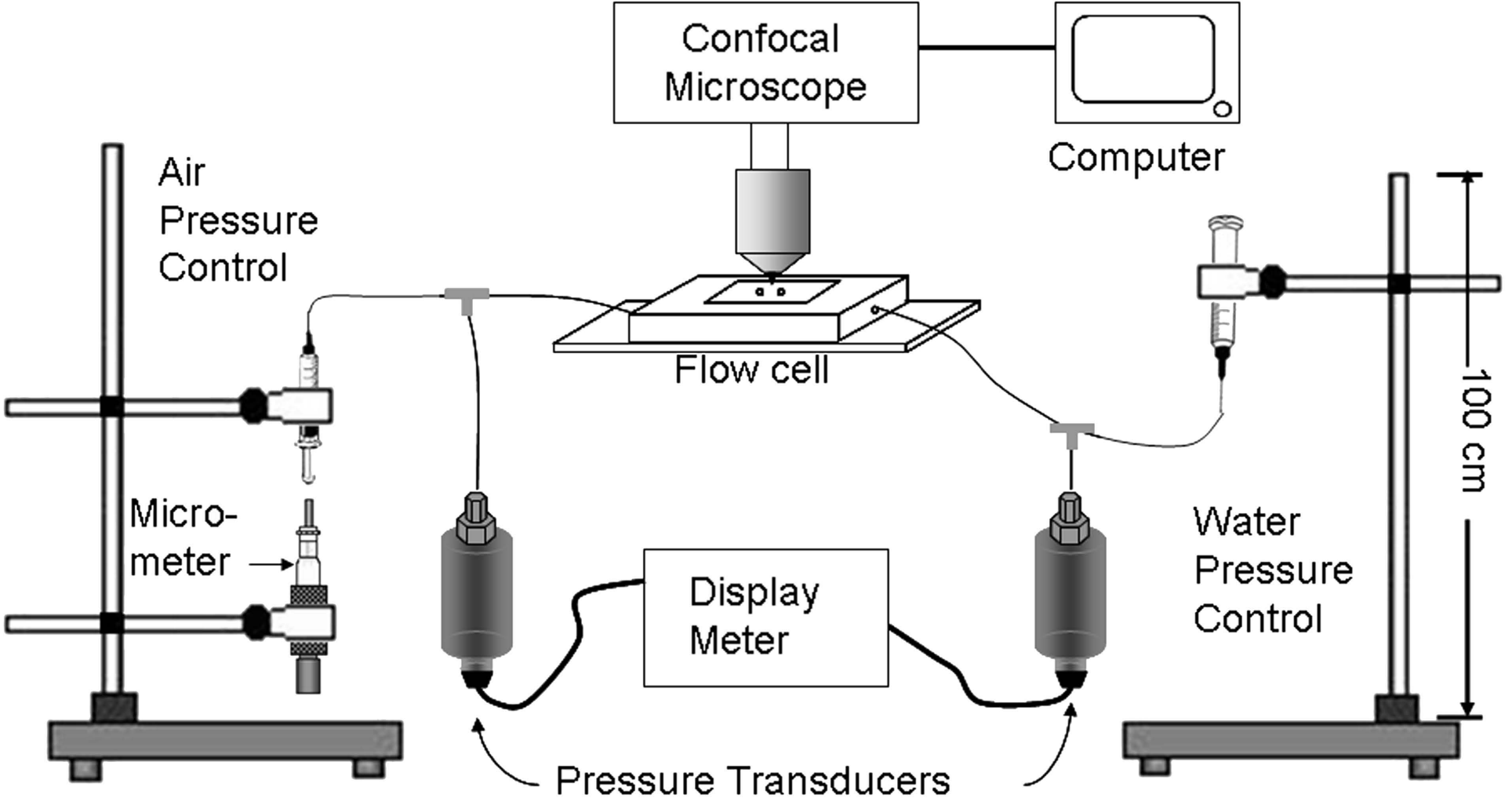
Confocal Microscope
Computer
Air Pressure Control
Flow cell
Micro-meter
Display Meter
Water Pressure Control
100 cm
Pressure Transducers

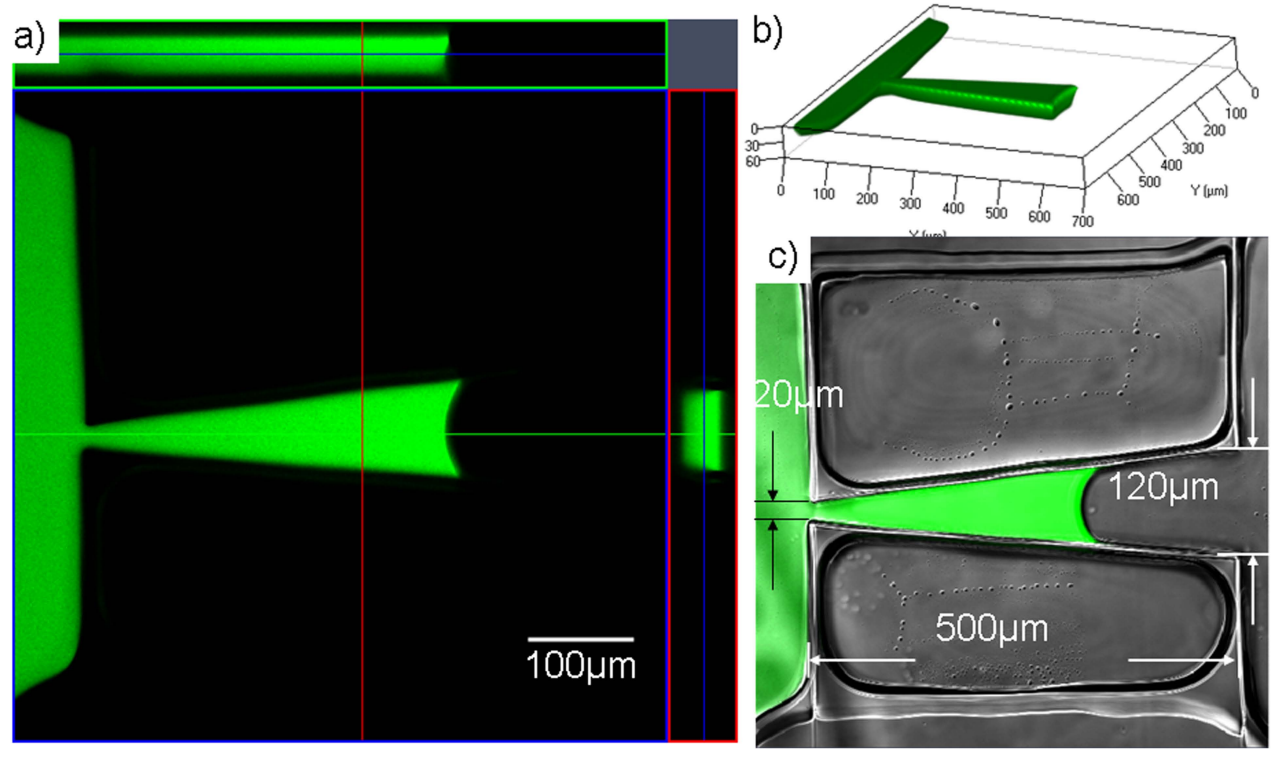
a)
100µm
b)
0
30
60
0
100
200
300
400
500
600
700
0
100
200
300
400
500
600
Y (µm)
c)
20µm
120µm
500µm

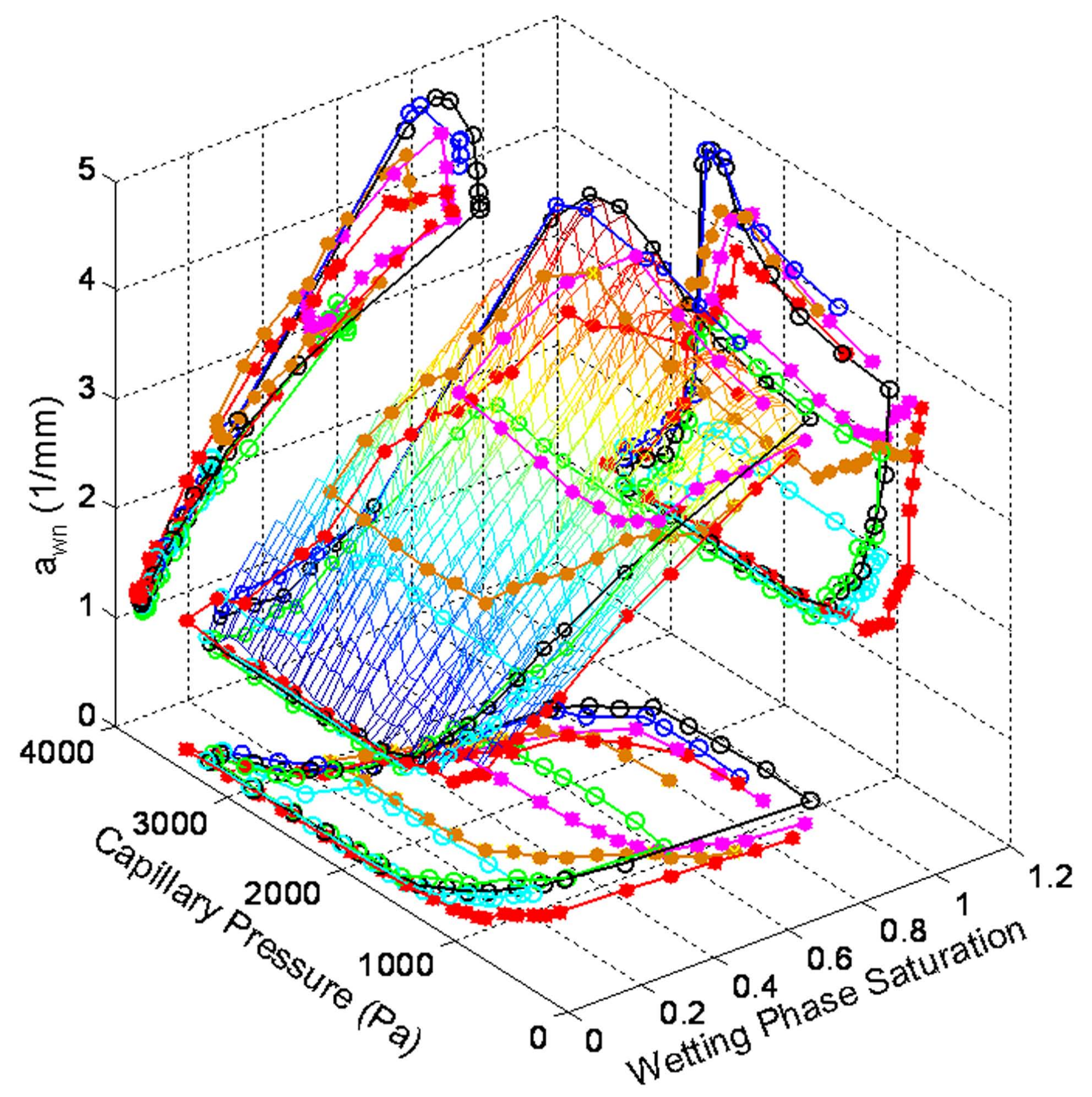
a_{wn} (1/mm)
5
4
3
2
1
0
4000
3000
2000
1000
0
Capillary Pressure (Pa)
0
0.2
0.4
0.6
0.8
1
1.2
Wetting Phase Saturation

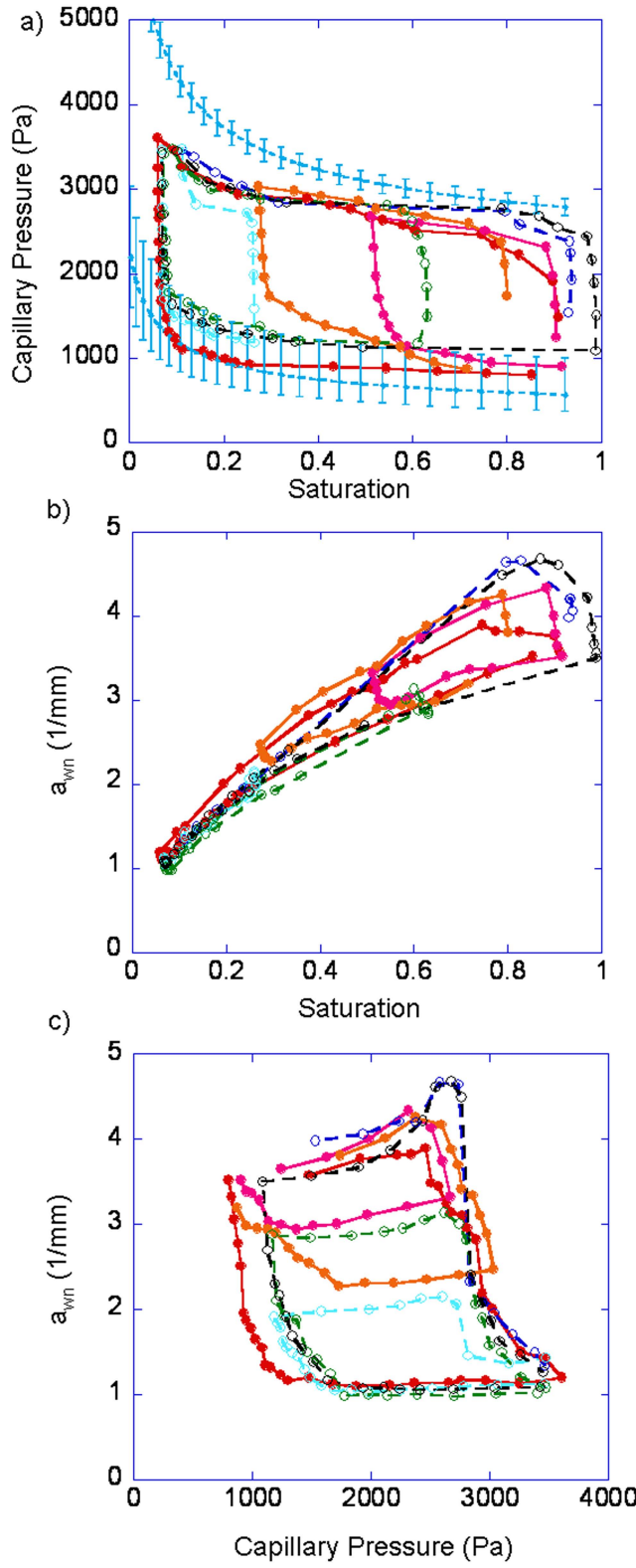
a)
Capillary Pressure (Pa)
5000
4000
3000
2000
1000
0
0
0.2
0.4
0.6
0.8
1
Saturation
b)
a_{wn} (1/mm)
5
4
3
2
1
0
0
0.2
0.4
0.6
0.8
1
Saturation
c)
a_{wn} (1/mm)
5
4
3
2
1
0
0
1000
2000
3000
4000
Capillary Pressure (Pa)

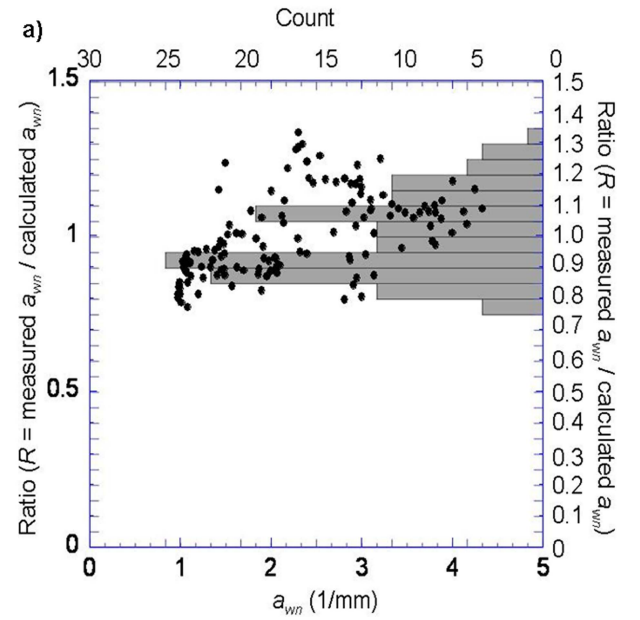
a)
Count
30
25
20
15
10
5
0
1.5
1
0.5
0
Ratio (R = measured a_{wn} / calculated a_{wn})
1.5
1.4
1.3
1.2
1.1
1.0
0.9
0.8
0.7
0.6
0.5
0.4
0.3
0.2
0.1
0
Ratio (R = measured a_{wn} / calculated a_{wn})
0
1
2
3
4
5
a_{wn} (1/mm)

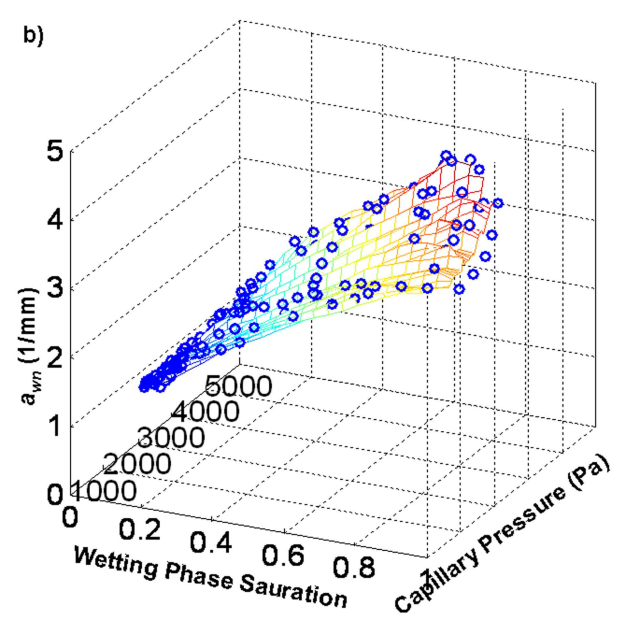
b)
5
4
3
2
1
0
a_{wn} (1/mm)
5000
4000
3000
2000
1000
0
0.2
0.4
0.6
0.8
1
Wetting Phase Sauration
Capillary Pressure (Pa)

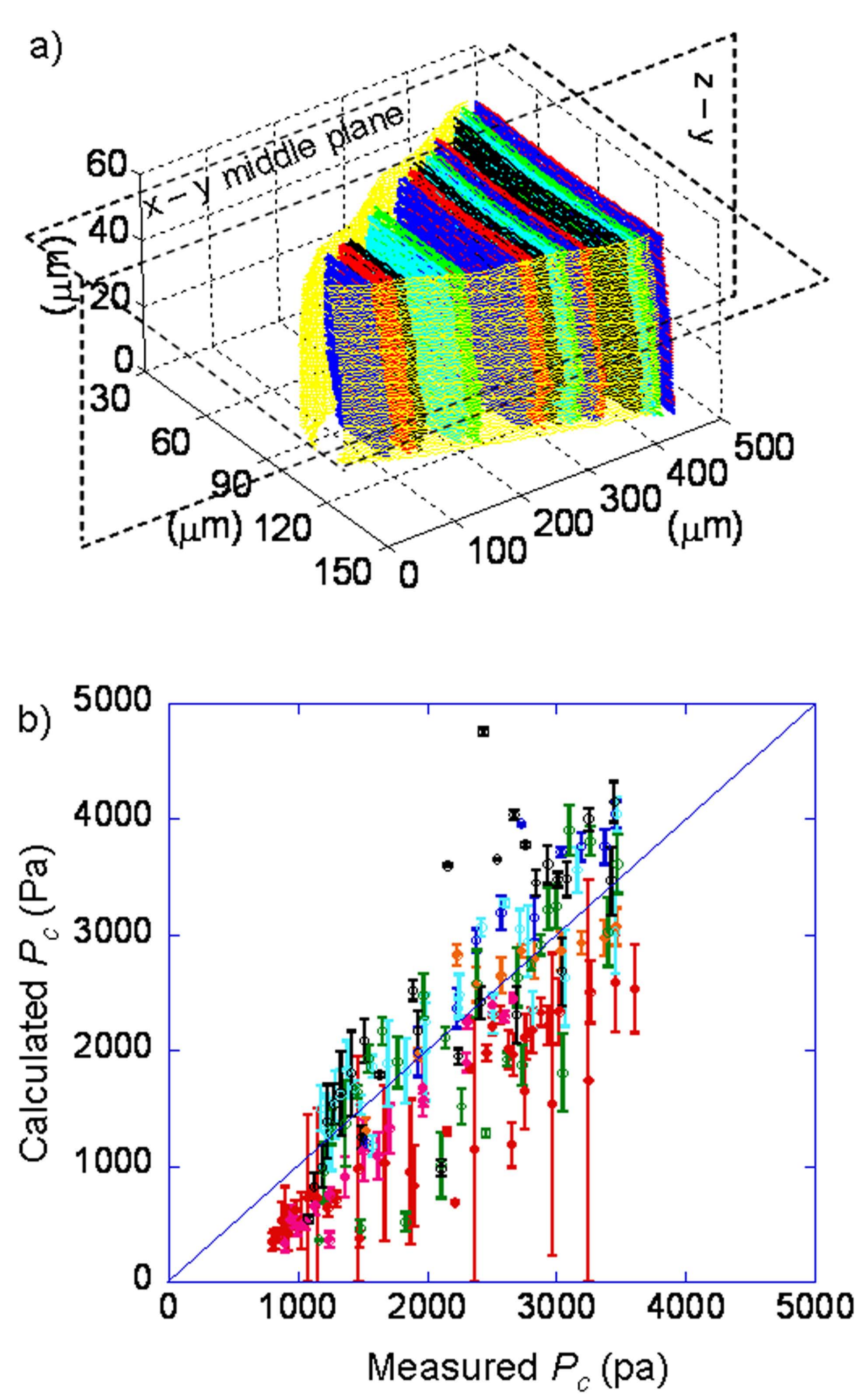
a)
x – y middle plane
z – y
60
40
20
0
(μm)
30
60
90
120
150
(μm)
0
100
200
300
400
500
(μm)
b)
5000
4000
3000
2000
1000
0
Calculated P_c (Pa)
0
1000
2000
3000
4000
5000
Measured P_c (pa)

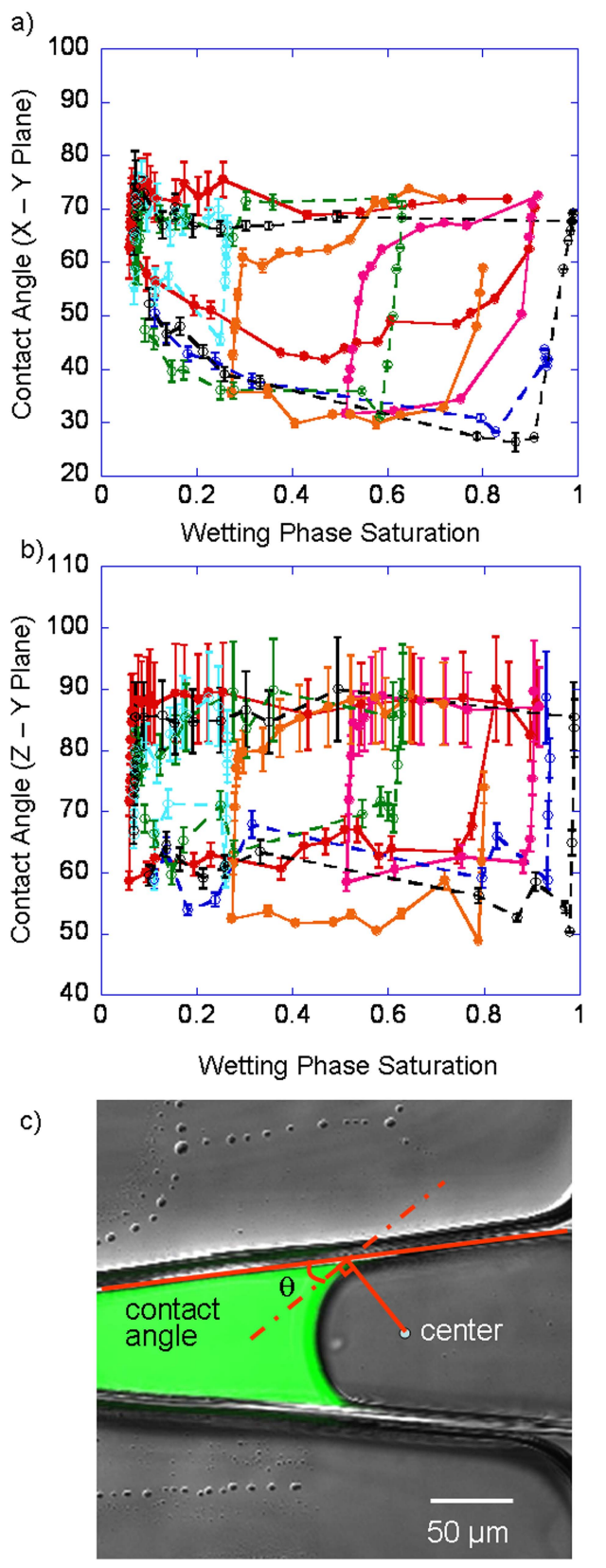
a)
Contact Angle (X – Y Plane)
100
90
80
70
60
50
40
30
20
0
0.2
0.4
0.6
0.8
1
Wetting Phase Saturation
b)
Contact Angle (Z – Y Plane)
110
100
90
80
70
60
50
40
0
0.2
0.4
0.6
0.8
1
Wetting Phase Saturation
c)
θ
contact
angle
center
50 µm

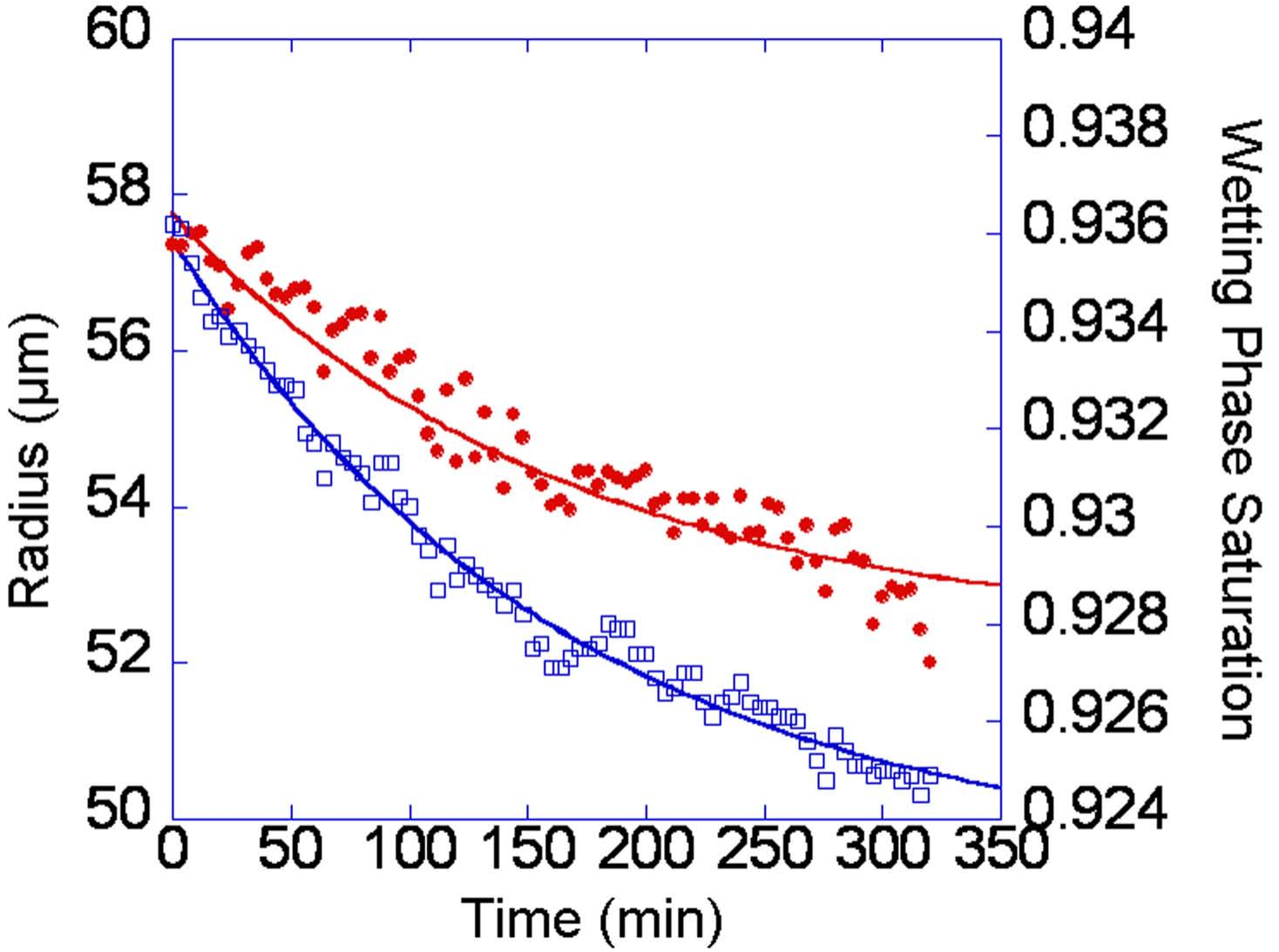
60
58
56
54
52
50
Radius (μm)
0.94
0.938
0.936
0.934
0.932
0.93
0.928
0.926
0.924
Wetting Phase Saturation
0
50
100
150
200
250
300
350
Time (min)

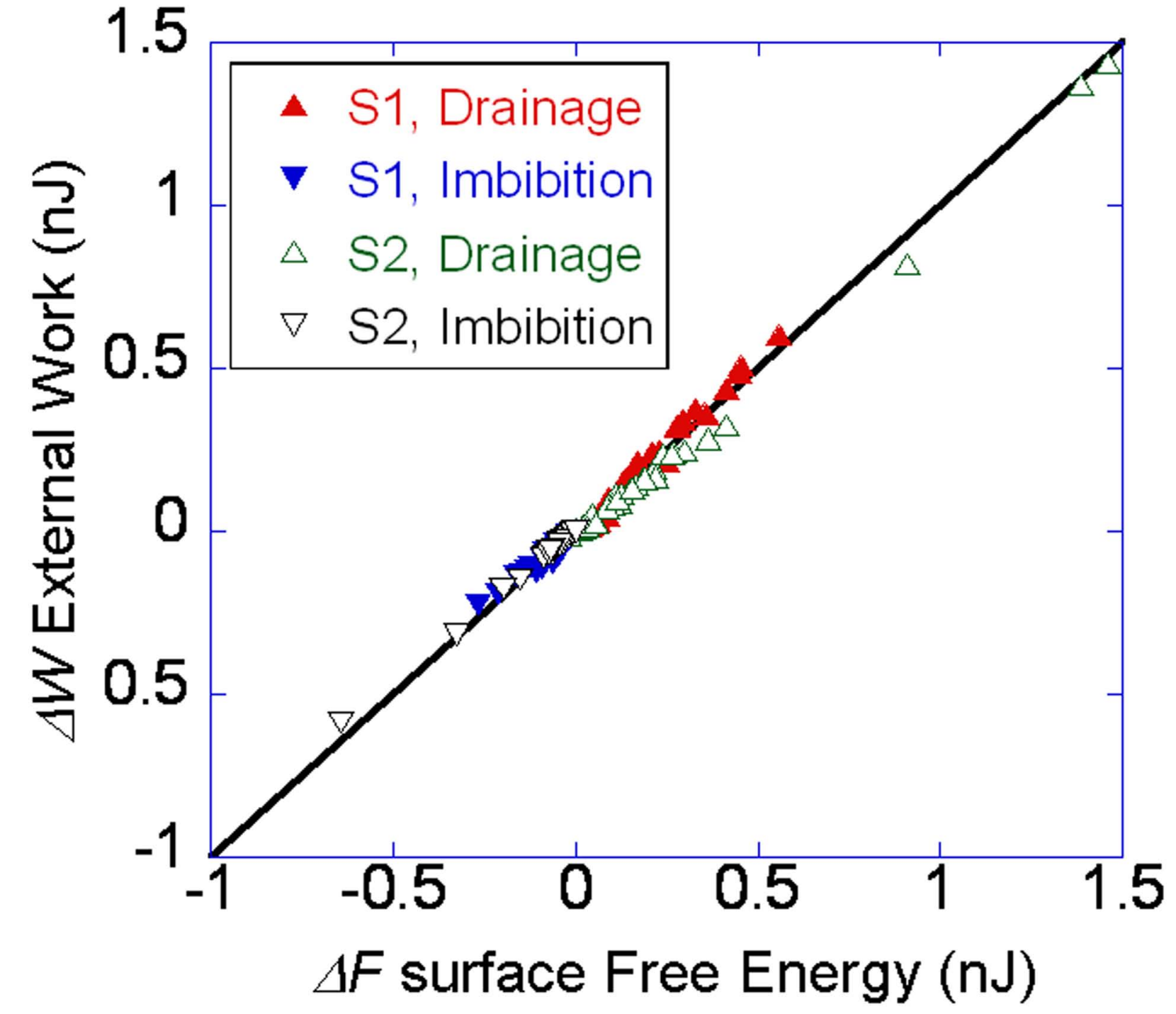
S1, Drainage
S1, Imbibition
S2, Drainage
S2, Imbibition
ΔW External Work (nJ)
ΔF surface Free Energy (nJ)
1.5
1
0.5
0
0.5
-1
-1
-0.5
0
0.5
1
1.5